(ASME Journal of Computational and Nonlinear Dynamics, Vol. 4(4) 2009)

Flight Dynamics and Simulation of Laser Propelled Lightcraft

Christopher G. Ballard*
NASA Jet Propulsion Laboratory, Pasadena, California 91109

Kurt S. Anderson†
Leik Myrabo ‡
Department of Mechanical, Aerospace and Nuclear Engineering
Rensselaer Polytechnic Institute
Troy NY 12180-3590

Abstract

A seven degree-of-freedom (DOF) dynamic model was developed to provide insight into the flight behavior of Type 200 and other related Lightcraft, and to serve as a research tool for developing future engine-vehicle configurations for laser launching of nano-satellites (1-10+ kg). Accurate engine, beam, and aerodynamics models are included to improve the predictive capability of the 7-DOF code. The aerodynamic forces of lift, drag, and aerodynamic pitching moment were derived from Fluent®computational fluid dynamics predictions, and calibrated against limited existing wind tunnel data. To facilitate 7-DOF model validation, simulation results are compared with video analysis of actual flights under comparable conditions. Despite current limitations of the 7-DOF model, the results compared well with experimental flight trajectory data.

*e-mail:Christopher.G.Ballard@jpl.nasa.gov
†Corresponding author: Department of Mechanical, Aerospace, and Nuclear Engineering; Rensselaer Polytechnic Institute, 110 8th Street, Troy, NY 12180-3590, USA; phone: 518-276-2339; fax: 518-276-2623; e-mail:anderk5@oceania.edu
‡e-mail:myrabl@rpi.edu

Nomenclature

$\hat{b}_1, \hat{b}_2, \hat{b}_3$	Dextral set of orthogonal unit vectors fixed in the despun reference frame(body)
$\vec{a}^{S^*}$	Acceleration of the mass center of the lightcraft with relative to the inertial reference frame
c	Reference chord
C_D	Coefficient of drag
C_L	Coefficient of lift
C_M	Aerodynamic Moment coefficient
$\sum \vec{F}$	Sum of all applied (external) nonimpulsive forces acting on the lightcraft
$\vec{G}$	Impulse imparted to the lightcraft by the laser
$\vec{\vec{I}}$	Central inertial dyadic of the lightcraft rotor
I^B_{ij}	ij element of the central inertia matrix of the despun platform (carrier) B, associate with the $\hat{b}$ basis
I^R	Central principal moments of inertial of the lightcraft rotor about directions $\hat{b}_2$ and $\hat{b}_3$
J^R	Central principal moment of inertial of the lightcraft rotor about direction $\hat{b}_1$
m	Mass of entire lightcraft
$\vec{M}^B$	Applied external moments to lightcraft carrier B
$\vec{M}^{R/B}$	Moments applied to lightcraft rotor R by carrier B
N	Newtonian reference frame
$\hat{n}_1, \hat{n}_2, \hat{n}_3$	Dextral set of orthogonal unit vectors fixed in the Newtonian reference frame
S	Reference surface area

S^*	Lightcraft system center of mass
v	Speed of the lightcraft relative to the flow
$\vec{v}$	Velocity of the lightcraft relative to the flow
α	Angle of attack (AOA)
δ	Dirac delta function
$\vec{\omega}$	Angular velocity of the despun lightcraft reference frame B relative to the Newtonian reference frame
$\vec{\dot{\omega}}$	Angular acceleration of the despun lightcraft reference frame relative to the Newtonian reference frame
ρ	density of the flow
$\dot{\psi}$	Spin rate of the lightcraft rotor relative to the despun lightcraft reference

1 Introduction

The lightcraft is an ultra-lightweight vehicle that employs a Beamed Energy Propulsion (BEP) engine linked to a ground-based laser power station. The Type 200 variant, which is the focus of most of the modelling and simulation work presented herein, is assembled from three parts: nose, annular shroud, and rear optic. The rear optic, which also serves as a plug nozzle, is an off-axis parabolic reflector that focuses incident pulsed laser energy into ring just beneath the shroud. Here, air or on-board solid ablative propellant is explosively heated by the focused laser pulse, and thrust is generated as high temperature, high pressure exhaust gases expand out the plug nozzle (Fig. 1). Between laser pulses the lightcraft coasts during which time the plasma/exhaust gases are vented and replaced by fresh air.

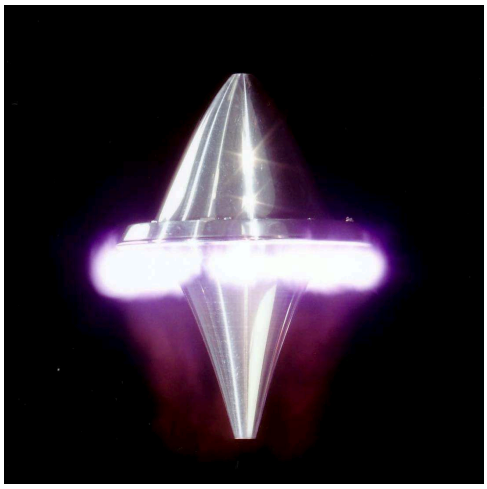

Figure 1: Laser induced air plasma with type 100 lightcraft

This Pulsed Detonation Engine (PDE) cycle has been extensively demonstrated in laboratory and outdoor flight experiments at White Sands Missile Range (WSMR) in New Mexico [1]. One lightcraft model in particular, the *Type 200*, has exhibited an unusual ability to "ride" the laser beam, consistently re-centering itself after being perturbed. Because of these characteristics, the #200-5/6 model lightcraft holds the current world altitude record of 71 meters set on October 2, 2000. In an attempt to improve the understanding of flight data, thrust performance, and beam-riding characteristics of the Type 200 lightcraft, an effort is underway to develop and validate a general physics-based simulation model that includes accurate dynamics, aerodynamics, engine, and laser beam models. The first attempt at modeling the flight dynamics with a 6-DOF code was performed by Libeau [2]. The ultimate goal is to produce a research tool that can facilitate invention of new lightcraft engine/vehicle geometries, assist creation of active flight control systems, and enhance understanding of experimental flight trajectories. Initial results from this multi-disciplinary, 7-DOF code development effort are summarized in the present paper.

2 Lightcraft Specifics

To date, all lightcraft flown at WSMR have been constructed from 6061-T6-511 aluminum as thin-shell (e.g., 0.245 mm wall thickness) bodies of revolution, completely symmetric about the vertically-oriented spin axis. In these demonstration flights, the vehicle was boosted by a 10 kW CO_2 electric discharge laser known as the Pulsed Laser Vulnerability Test System (PLVTS), located on the High Energy Laser System Test Facility (HELSTF) at WSMR. The laser produces a hollow square beam profile whose dimensions can be varied with telescope-like optics to match the size of the lightcraft shroud. The propulsive reaction received by the lightcraft system from repetitive laser-induced detonations embodies three linear impulses and three angular impulses. However, of these, only the thrust impulse, side (restoring) impulse, and pitching angular impulse dominate the craft's flight behavior. The thrust impulse propels the vehicle skyward, whereas the side impulse attempts to center the lightcraft in the laser beam; the pitching impulse, which results from a lateral offset, tends to tip the vehicle. To minimize effects from this pitching impulse, and to prevent tumbling, the lightcraft is spun to approximately 10,000 RPM about its axis of symmetry prior to launch. This initial spin rate stabilized the lightcraft, and provides the additional benefit of insuring that the proportion of the reflector being illuminated by a particular portion of the beam is always changing. This distribution of beam energy is important because local "hot spots" in the beam would more quickly result in localized engine overheating and burn through. Additionally, the spinning of the lightcraft relative to the flow, greatly increases convective cooling of the reflector, and prolongs reflector life.

In the straight airbreathing mode, superheated air is the only propellant, and the and

focal region of the lightcraft optic begins to heat up almost immediately. The overheating of the lightcraft "engine" is marked by a significant drop in thrust as beam energy goes into the heating of the engine material instead of the air which provides thrust. This overheating becomes catastrophic as the optic focal region begins to melt, resulting in the near total loss of thrust and the destruction of the lightcraft model.

To improve engine thrust beyond that attainable with the airbreathing mode, a solid ablative propellant ring of Delrin® is inserted into the annular shroud at the focus of the primary optic. Not only does this propellant increase engine thrust by a factor of 2.5, but the ablating Delrin® helps to cools the shroud. Without such cooling, the aluminum shroud predictably fails at the 100th laser pulse-e.g., after 4 seconds of operation at 25 Hz with 420 Joule pulses. Hence, all altitudes beyond 30 m have used Delrin®. The Type 200 lightcraft currently under development serves as a research craft for evolving future laser-propelled launch vehicles with superior performance.

3 Model Development

The present seven degree-of-freedom model represents the spinning lightcraft as a gyrostat [3], shown schematically in figure 2. This represents a "despun" payload compartment/carrier B with mass center B^*; a symmetric spinning rotor R, with mass center R^*; and the system center of mass S^*, all located relative to a well established design reference point P, and dextral basis vectors $\hat{b}_1$, $\hat{b}_2$, $\hat{b}_3$, fixed in reference frame (body) B. For all cases considered here the rotation axis of the rotor is defined to be parallel to direction $\hat{b}_1$, which is nominally the preferred flight direction. The carrier is then acted upon by laser impulses,

gravity and aerodynamic loads. This model has been produced with the intent of treating planned future lightcraft which will include such a despun equipment/crew platform, and been constructed for simulating and testing various proposed active reaction control systems.

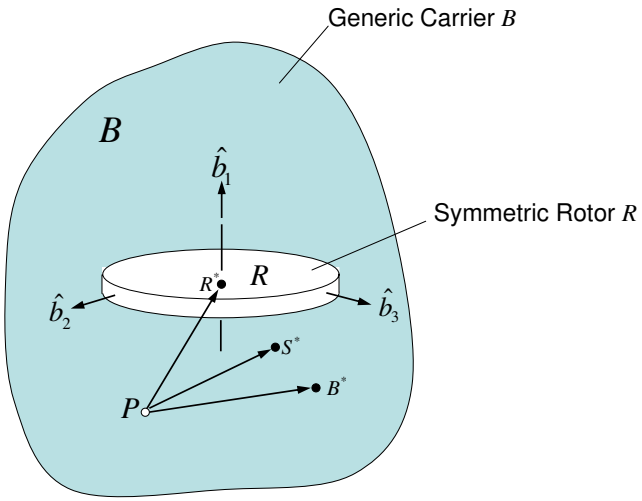

Figure 2: Generic craft rotor system

The equations of motion for this system are

$$
\left\{ \begin{array}{c} M_1^B \\ M_2^B \\ M_3^B \\ M_1^{R/B} \end{array} \right\} = \left[\begin{array}{cccc} I_{11}^B & I_{12}^B & I_{13}^B & J^R \\ I_{12}^B & (I_{22}^B + I^R) & I_{23}^B & 0 \\ I_{13}^B & I_{23}^B & (I_{33}^B + I^R) & 0 \\ J^R & 0 & 0 & J^R \end{array} \right] \left\{ \begin{array}{c} \dot{\omega}_1 \\ \dot{\omega}_2 \\ \dot{\omega}_3 \\ \ddot{\psi}_3 \end{array} \right\}
$$
$$
+ \left\{ \begin{array}{c} (I_{13}^B\omega_2 - I_{12}^B\omega_3)\omega_1 + (I_{23}^B\omega_2 - I_{22}^B\omega_3)\omega_2 \\ (I_{11}^B\omega_3 - I_{13}^B\omega_1)\omega_1 + (I_{12}^B\omega_3 - I_{23}^B\omega_1)\omega_2 \\ (I_{12}^B\omega_1 - I_{11}^B\omega_2)\omega_1 + (I_{22}^B\omega_1 - I_{12}^B\omega_2)\omega_2 \\ 0 \end{array} \right\}
$$
$$
+ \left\{ \begin{array}{c} (I_{33}^B\omega_2 - I_{23}^B\omega_3)\omega_3 \\ (I_{13}^B\omega_3 - I_{33}^B\omega_1)\omega_3 + J^R\omega_3\dot{\psi} + (J^R - I^R)\omega_1\omega_3) \\ (I_{23}^B\omega_1 - I_{13}^B\omega_2)\omega_3 - J^R\omega_2\dot{\psi} + (I^R - J^R)\omega_1\omega_2) \\ 0 \end{array} \right\} \tag{1}
$$

where I_{ij}^B represents the ij element of the central inertial matrix of despun platform/carrier B, with angular velocity relative to the Newtonian frame N of $\vec{\omega}^B = \omega_1\hat{b}_1 + \omega_2\hat{b}_2 + \omega_3\hat{b}_3$. $\vec{M}^B = M_1^B\hat{b}_1 + M_2^B\hat{b}_2 + M_3^B\hat{b}_3$ is the sum of all external moments applied to the carrier B from outside the system, while $M_1^{R/B}$ is the $\hat{b}_1$ component of the moment exerted on the rotor R by the carrier B. The moments $\vec{M}^B$ arise from laser pulse loads, aerodynamic loads, and thruster firings associated with a proposed reaction control system. The quantity I^R is the central moment of inertia associated with the directions $\hat{b}_2$ and $\hat{b}_3$, while J^R is the rotor central moment of inertia about the spin axis $\hat{b}_1$. Lastly, the angular velocity of the rotor R relative to the carrier B is $\dot{\psi}\hat{b}_1$.

Each load acting on the lightcraft is determined from a engineering models which have been developed for this purpose. These forcing term models take in the lightcraft state and return the corresponding forcing values. The different models used for this purpose may be briefly described as:

Gravity - Gravity forces are determined using an inverse square gravitational field and is adjusted as needed to correctly consider the lightcraft altitude and motion, particularly as it pertains to achieving orbital trajectories.

Laser Thrust Forces and Moments - The laser pulses generate axial thrusts and tipping moments, as well as restoring (lateral) forces which act to push the lightcraft back toward the center of the beam giving the Mark 200 family of lightcraft their inherent beam riding capabilities. The thrust, as well as the laser pulse generated restoring forces and tipping moments are determined from the "engine" and "beam" models working in conjunction given the state of the system as output from the dynamics model.

The *Beam Model* determines the beam energy flux [joules/m^2] as a function of location in the beam. This flux varies both with the position within the beam cross section, and the distance along the beam. The optics of the laser permit the beam limited transverse motion, and the laser focal point may also be moved in a controlled fashion along the beam.

The *Engine Model* - The energy flux associated with a laser pulse entering the optic is integrated over the optic, yielding the total laser energy captured by the optic for the laser pulse being considered. Additionally, the engine-beam model then determines

the centroid of this distributed energy pulse within the optic. The engine model then utilizes these captured energy and energy centroid location estimates within the optic for the given laser pulse to produce values for the translational and rotation impulses imparted to the lightcraft by the pulse. The model used is a parameterization of experimental data collected in [2].

Aerodynamic Loads - The aerodynamic drag D_A, lift L_A, and tipping moment M_A, used in this treatment are modeled as

$$D_A = \frac{1}{2}\rho v^2 S C_D \tag{2}$$

$$L_A = \frac{1}{2}\rho v^2 S C_L \tag{3}$$

$$M_A = \frac{1}{2}\rho v^2 S C_M \tag{4}$$

.

Within these equations, ρ is the local air density, v is of the speed of the craft relative to the air flow, and S is the planform area, while C_D, C_L, and C_M are the aerodynamics coefficients of drag, lift, and pitching moment, respectively. These aerodynamic forces are then applied to the light in the convention indicated in figure (3).

The aerodynamic lift, drag, and pitching moment coefficient behavior vs. the angle of attack (AOA) α [rad] for a non-spinning lightcraft were obtained from Fluent CFD simulations by McInerny [4]. This aerodynamic database was then parameterized for efficient use in the computer model. Analytical curve-fits of each coefficient were derived for angles of attack α from zero to ninety degrees; the latter is necessary for

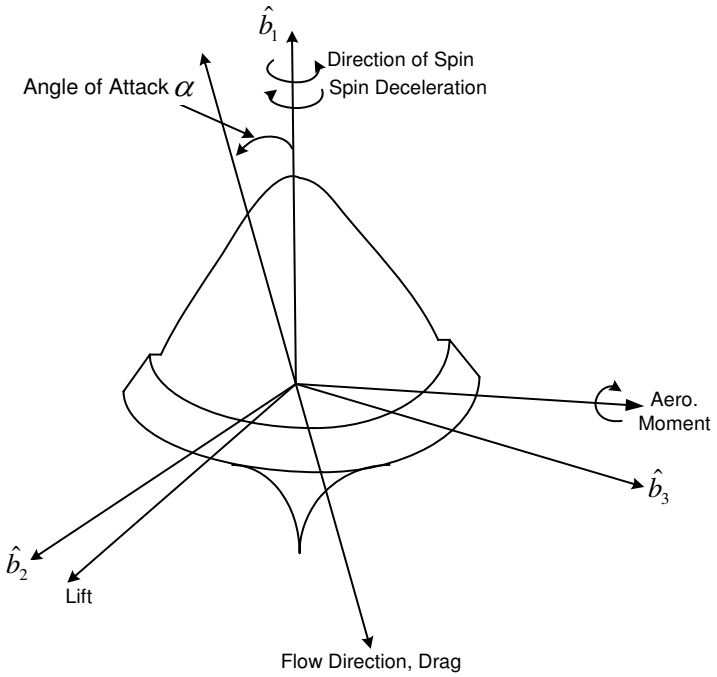

Figure 3: Lightcraft aerodynamic loads diagram

simulating hovering flights with crosswinds. The polynomial approximations which best fit these data are

$$\begin{aligned} C_D &= 0.3928\alpha^3 - 0.8463\alpha^2 + 0.0398 * \alpha + 0.731, \\ C_L &= 0.1993\alpha^5 - 0.3317\alpha^4 - 0.2724\alpha^3 \\ &\quad +0.5531\alpha^2 + 0.5531\alpha, \\ C_M &= 0.1598\alpha^6 - 0.6619\alpha^5 + 8794\alpha^4 \\ &\quad -0.3585\alpha^3 - 0.0583\alpha^2 + 0.080\alpha. \end{aligned} \tag{5}$$

Figures 4, 5, and 6 show the curve-fits (solid line) associated with the of actual CFD data (discrete data markers). Polynomial fits of various orders were investigated (third order to sixth order) as well as the use of Hermite spline interpolation. The the

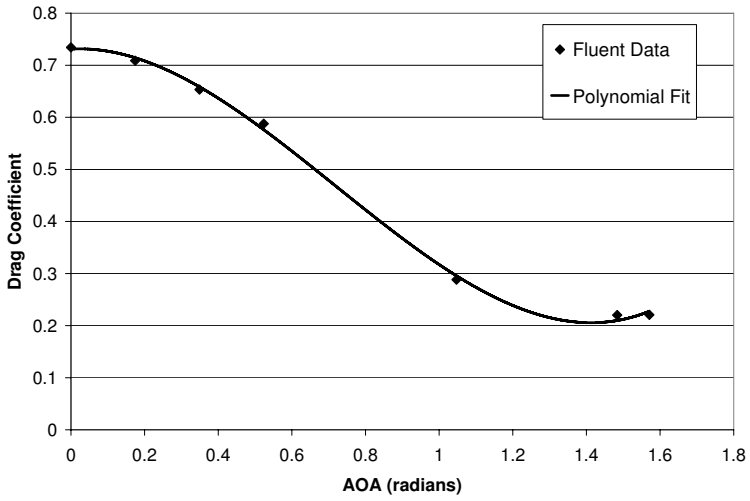

Figure 4: Lightcraft aerodynamic drag coefficient vs. angle of attack

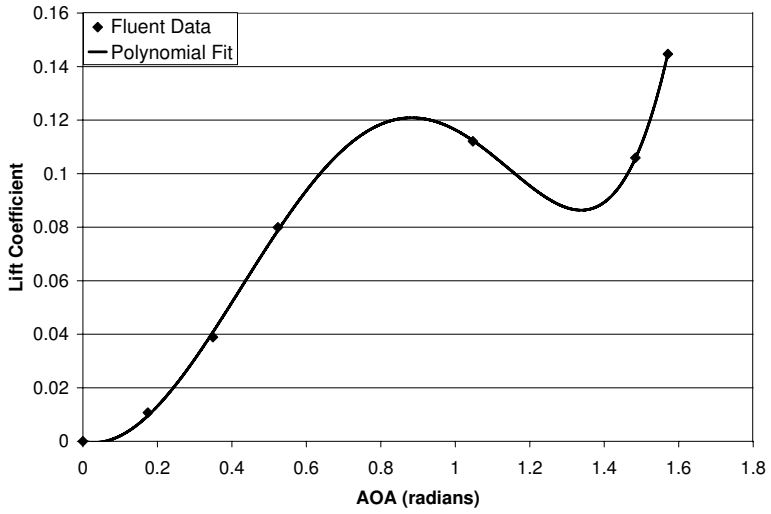

Figure 5: Lightcraft aerodynamic lift coefficient vs. angle of attack

lowest order polynomials fits were chosen which were felt to adequately match the obtained data. It is recognized that the use of high order polynomial fits may result in oscillatory behavior which is not real. Additionally, some sizable gaps exist in the Fluent generated case studies. Filling those caps and improving the parameterization

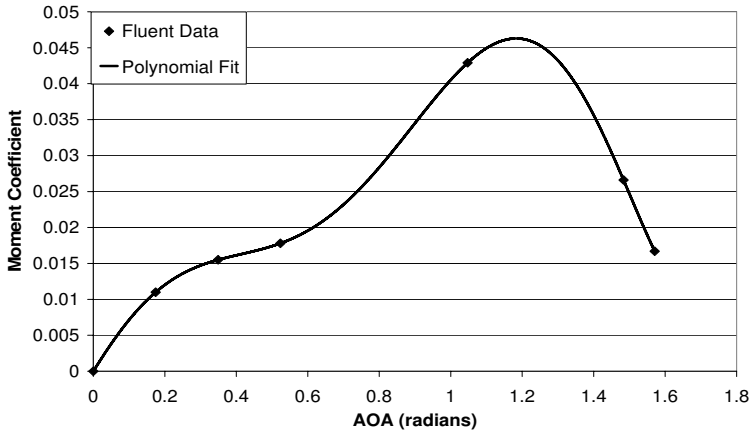

Figure 6: Lightcraft aerodynamic moment coefficient vs. angle of attack

of these aerodynamic terms is the topic of current on going work.

Additionally, the spin deceleration of the craft due to aerodynamics drag was also approximated by an exponential decay function, with the decay rate obtained from laboratory experiments. The spin deceleration is realized by the application of an appropriate aerodynamic moment T about the spin axis and is given by

$$T = J\dot{\omega}_1. \tag{6}$$

Reaction Control System (RCS) - The associated dynamics model finally includes the ability to place RCS thrusters at any location and with any specified orientation on the lightcraft. Given the RCS thruster location, orientation, and thrust level, the appropriate forces and associated moments are automatically applied to the system with the mass properties of the lightcraft being adjusted to properly account for RCS propellant usage.

All the simulations discussed in this paper are associated with experimental flights,

and lack a RCS system. The RCS capability was added such that this simulation tool, once validated could be used to aid in the design of the future lightcraft versions which are expected to possess active reaction control.

For all lightcraft so far built and flown, the entire system acts as the rotor. The "despun" platform B is thus a massless reference frame and the system degenerates to a six degree-of-freedom spinning, axially symmetric body, where the rotor rotation rate relative to B is a prescribed $\dot{\psi}$. For this idealized system, the rotational equations of motion for the lightcraft then take the form

$$\begin{aligned}\vec{M}^B = [J^R\dot{\omega}_1]\hat{b}_1 \quad &+ \quad [I^R\dot{\omega}_2 + (J^R - I^R)\omega_3\omega_1 + J^R\omega_3\dot{\psi}]\hat{b}_2 \\ &+[I^R\dot{\omega}_3 - (J^R - I^R)\omega_1\omega_2 - J^R\omega_2\dot{\psi}]\hat{b}_3. \end{aligned} \tag{7}$$

For the results presented here, the lightcraft body spins at a constant rate with respect to a "despun" reference frame about the craft axis of symmetry. This despun reference frame nominally has a nonzero angular velocity $\vec{\omega} = \omega_1\hat{b}_1 + \omega_2\hat{b}_2 + \omega_3\hat{b}_3$, but is termed "despun" because $\omega_i \ll \dot{\psi}$ $(i = 1, 2, 3)$. The angular velocity of the lightcraft rotor with respect to the Newtonian (inertial) reference frame is then given by

$$\vec{\omega}^R = (\omega_1 + \dot{\psi})\hat{b}_1 + \omega_2\hat{b}_2 + \omega_3\hat{b}_3. \tag{8}$$

And the system angular acceleration is

$$\vec{\dot{\omega}}^R = (\dot{\omega}_1 + \ddot{\psi})\hat{b}_1 + (\dot{\omega}_2 + \omega_3\dot{\psi})\hat{b}_2 + (\dot{\omega}_3 - \omega_2\dot{\psi})\hat{b}_3 \tag{9}$$

This form of the model exploits system symmetries and permits significantly larger temporal integration steps to be taken while maintaining both integrator stability and accuracy which was not done in [2]. The model was created using Autolev® [5], a dynamic modeling software that uses Kane's method [6] to develop the equations of motion. The actual mathematical model on which the associated simulation code was produced is significantly more general than this, permitting the masses and associated mass properties of the carrier and/or rotor to vary with time, permitting the accurate consideration of propellant usage.

To accurately capture the behavior of future lightcraft flights to extreme altitudes, the Newtonian reference frame, with associated basis vectors $\hat{n}_1, \hat{n}_2, \hat{n}_3$, was taken to be the standard de-spun Earth reference frame [7] placed at the Earth's center and aligned such that $\hat{n}_1$ points outward toward the vernal equinox, $\hat{n}_3$ points outward along the Earth's rotation axis toward the north geometric pole, and $\hat{n}_2 = \hat{n}_3 \times \hat{n}_1$. The model uses an inverse square law gravitational field, and correctly accounts for centripetal and Coriolis acceleration variation with launch site location. Additionally, model state variables are defined with respect to the launch site reference frame (i.e., fixed at the launch point) as opposed to the despun system inertial frame, so that simulated quantities (position, velocity, and acceleration) may be directly related to the associated quantities measured experimentally at the launch site. The vehicle mass, center of mass, and mass moments of inertia may vary with time to account for the consumption/ablation of rocket propellant. The ablation rate was empirically determined and relates grams ablated propellant to the Joules collected from the laser beam within the lightcraft optic. The model can additionally simulate the behavior of lightcraft under the influence of a crosswind that is variable in both magnitude and direction.

If t_k is the time at which the impulsive thrust occurs, then the lightcraft translational

equation of motion may be written as

$$\vec{F_N} + \vec{G}_F \delta(t - t_k) = m\vec{a}^{S^*} \tag{10}$$

and the rotational equations become

$$\begin{aligned} \vec{M_N^B} + \vec{G_M^B}\delta(t - t_k) = [J^R\dot{\omega}_1]\hat{b}_1 \quad + \quad & [I^R\dot{\omega}_2 + (J^R - I^R)\omega_3\omega_1 + J^R\omega_3\dot{\psi}]\hat{b}_2 \\ & +[I^R\dot{\omega}_3 - (J^R - I^R)\omega_1\omega_2 - J^R\omega_2\dot{\psi}]\hat{b}_3. \end{aligned} \tag{11}$$

In these equations the terms $\vec{F_N}$ and $\vec{M_N^B}$, respectively, represent is the sum of all applied non-impulsive forces and moments acting of the lightcraft. These terms include gravitational forces, aerodynamic loads, and the forces and moments resulting from the firing of the Reaction Control System (RCS). Similarly, $\vec{G}_F$ and $\vec{G_M^B}$ are associated with the impulsive forces and moments, respectively, imparted to the lightcraft by the laser. In general these are a complex function of system geometry (optic size and shape, orientation, location in the beam, and laser beam profile), air density, and the ablative propellant. $\delta(t - t_k)$ is the Dirac delta function, m the mass of the lightcraft at time t, and $\vec{a}^{S^*}$ is the acceleration of the center of mass of the lightcraft with respect to the inertial reference frame.

During the majority of each launch, the laser is off between very brief pulses/firings of nominally $1.8 \times 10^{-}5$ second duration at a pulse rate of 25-27 Hz. This allows the plasma and ablated propellent which is created by the prior laser pulse to vent and fresh air to enter the "combustion" region of the optic before the next laser discharge. As such the laser pulses are active only 0.045% of the time, so their treatment as impulsive in this model is valid. This being the case the laser impulsive terms in eqns. 10 and 11 are not considered except

at times t_k, and the equations of motion may be integrated directly by conventional means. However, at times t_k the very large and rapidly changing thrust terms will be difficult to temporally integrate properly.

To circumvent these numerical temporal integrations difficulties at time t_k the simulation code has be written such that it does not need to actually integrate through these laser pulses. If it is determined that a laser pulse will occur during the next temporal integration step, then that integration step size is adjusted so that the step will finish at $t_k \pm \epsilon$, where ϵ was nominally 10^{-6} seconds. At this time the impulse-momentum equations for the system may be compactly written as

$$\underbrace{\int_{t_k^-}^{t_k^+} \left(\vec{F_N}\right) dt}_{\sim 0} + \underbrace{\int_{t_k^-}^{t_k^+} \vec{F_T} dt}_{\text{bounded}} = \int_{t_k^-}^{t_k^+} \left(m\vec{a}^{S^*}\right) dt \tag{12a}$$

$$= m\vec{v}^{S^*}\big|_{t_k^+} - m\vec{v}^{S^*}\big|_{t_k^-} \tag{12b}$$

and

$$\underbrace{\int_{t_k^-}^{t_k^+} \left(\vec{M}_N\right) dt}_{\sim 0} + \underbrace{\int_{t_k^-}^{t_k^+} \vec{M}_T dt}_{\text{bounded}} = \underbrace{\int_{t_k^-}^{t_k^+} \left(J^R \dot{\omega}_1 \hat{b}_1 + I^R[\dot{\omega}_2 \hat{b}_2 + \dot{\omega}_3 \hat{b}_3]\right) dt}_{\text{bounded}} \tag{13a}$$

$$+ \underbrace{\int_{t_k^-}^{t_k^+} \left([(J^R - I^R)\omega_3\omega_1 - J^R\omega_3\dot{\psi}]\hat{b}_2 - [(J^R - I^R)\omega_1\omega_2 + J^R\omega_2\dot{\psi}]\hat{b}_3\right) dt}_{\sim 0}$$

$$= \left(J^R\omega_1\hat{b}_1 + I^R[\omega_2\hat{b}_2 + \omega_3\hat{b}_3]\right)\big|_{t_k^+} - \left(J^R\omega_1\hat{b}_1 + I^R[\omega_2\hat{b}_2 + \omega_3\hat{b}_3]\right)\big|_{t_k^-} \tag{13b}$$

The first term on the left-hand side of equation (12a) vanishes because the integrand $\vec{F_A}$ is bounded, and the duration of the integration is effectively zero. The second term on the left-hand side of equation (12a) is the impulse imparted to the system resulting from the laser pulse, and is determinable from the combined engine-beam models using the known system

geometry, local air properties and propellant type. The second term on the right-hand side of equation (12b) is known from system state at time t_k^-, as is $m|_{t_k^+}$. Consequently, the only unknowns in equation (12b) are the values associated with the components of $\vec{v}^{S^*}\big|_{t_k^*}$, which may be immediately solved for.

Similarly, the first term on the left-hand side of equation (13a) vanishes because the integrand $\vec{M}_A$ is bounded, and the duration of the integration is effectively zero. The second term on the left-hand side of equation (13a) is the rotational impulse imparted to the system resulting from the laser pulse, and is determinable from the engine-beam models and the system state. The second term on the right-hand side of equation (13a) is also zero because its integrand is similarly bounded. Finally, the second term on the right-hand side of equation (13b) is known from the system state ar time t_k^-, as is are the inertial values. Consequently, the only unknowns in equation (13b) are the values associated with the components of $\vec{\omega}^B\big|_{t_k^*}$, which may be immediately determined.

The mass and mass moments of inertia for lightcraft that flew at WSMR were experimentally determined from laboratory tests, and agree with estimates obtained using the solid modeling package Solid Works [8]. Lightcraft flight trajectory data (3-D position vs. time) were extracted from WSMR camcorder videos that tracked both the vertical position and lateral position (i.e., "gun camera" view) within the laser beam.

Figure 7 demonstrates that the couple aerodynamics/engine-beam models function as expected, and reveals the behavior of a #200-3/4 SAR lightcraft under the influence of gravity, axial laser impulses, and aerodynamic drag. Each jump in axial velocity is associated with a laser pulse and the magnitude of each jump correlates with the beam intensity for the given system geometry (orientation of the lightcraft, as well as its position (x, y, z coordinates) in

the beam). The drag behaves in a similar way, with the force increasing with square of the flow speed.

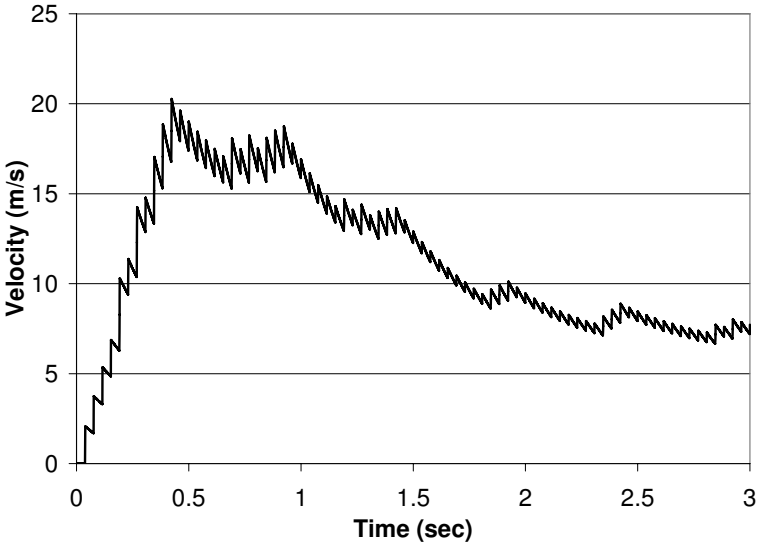

Figure 7: Characteristic vertical speed of #200-3/4 SAR lightcraft (simulation of flight 16)

4 Comparison With Flight Data

Lightcraft flight trajectory data was extracted from WSMR videotapes using *ImageExpress* software. This experimental performance was then compared to the degenerate 6-DOF model simulations run under similar conditions (see Table 1). The experimental results were obtained using the PLVTS 10 kW CO_2 electric discharge laser with pulse rates ranging from 25-27 Hz and a pulse width of 18μs. Figure 9 shows a comparison of climb performance for an airbreathing PDE flight of the #200-5/6 with the simulation. The code simulation compares well with the flight for the full 2.5 seconds of available flight data. To capture the experimental data this well, an engine overheating model had to be included with the overall

engine model to predict the decrease in thrust due to engine overheating.

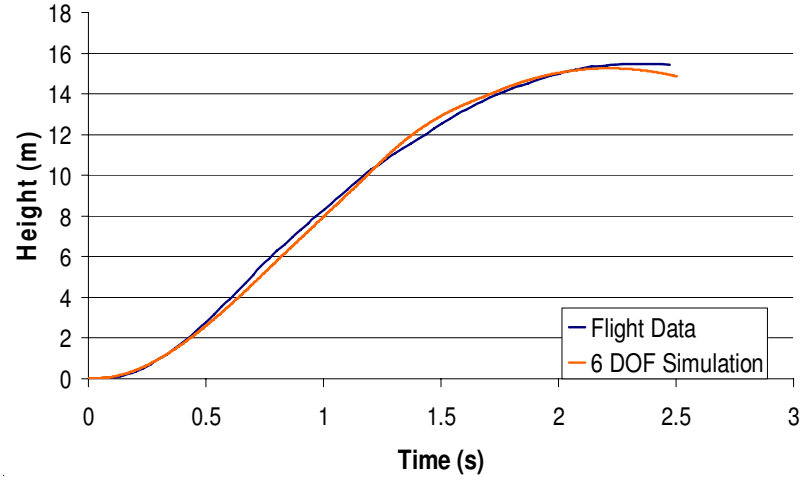

Figure 8: Model comparison of #200-5/6 lightcraft in airbreathing PDE mode (flight 5)

Figure 9 shows a similar comparison for a Delrin PDE flight (i.e., #200-3/4SAR) for which the agreement between experimental flight and simulation performance is very good. The simulations in each case had to correctly account for the lightcraft optic position (orientation and location) within the beam along the flight path. This was critical to obtaining good results because lightcraft was not able to capture all of the power along the flight path. In effect the power "spills" over the sides of the engine, and the beam intensity varies significantly with location within the beam. Since the engine model is based on laboratory experimental data, the fact that so much power is not taken in is significant. This level of agreement between experiment and simulation results is surprising, given the relative simplicity of the engine and beam propagation models used in at this point in the simulation. More recent trial simulations with improved (albeit still simplified) beam and engine models appear to match even finer scale variations in flight trajectory data.

Most importantly, this lightcraft systems model, comprised now of couple dynamics,

Parameter	Airbreathing Mode Flight 5	Solid Abative Rocket Mode flight 16
Lightcraft Model	#200-5/6	#200-3/4
Propellant	air	Delrin
Vehicle Diameter (mm	122.2	109.9
Vehicle Launch Mass (g)	32.5	29.02
Moment of Inertia: J ($g - cm^2$)	602.7	364.2
Moment of Inertia: I ($g - cm^2$)	465.3	293.9
Time-Average Laser Power (kW)	10	4.2
Initial Laser Pulse Energy (J)	420	420
Pulse Repetition Frequency (Hz)	26	25
Vehicle Drag Coefficient	0.731	0.731
Launch Altitude (m)	1194	1194
Initial Laser Engine Impulse (N-s)	0.0637	0.195
Initial Laser Beam Size (cm)	7.1974	5.8239

Table 1: Lightcraft parameters and flight conditions

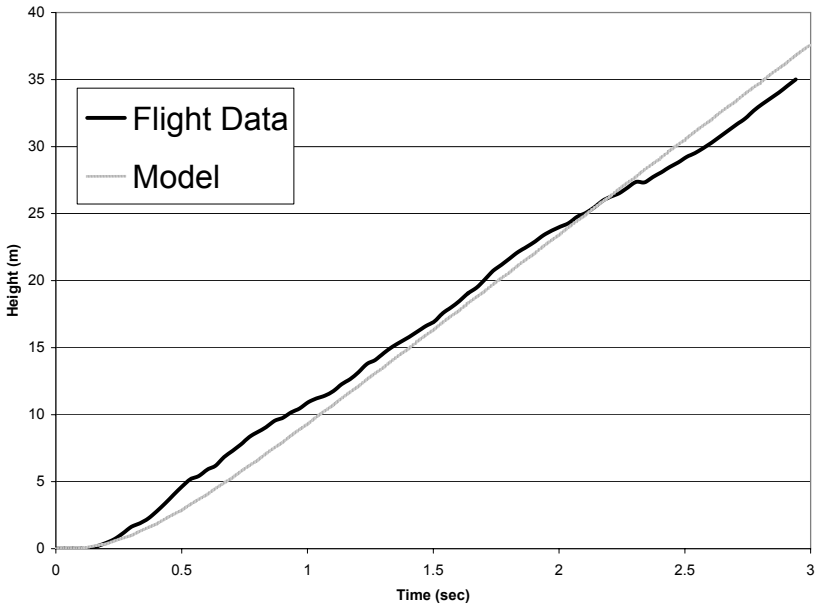

Figure 9: Model comparison of #200-3/4SAR lightcraft in Solid Ablative Rocket (SAR) mode (flight 16)

aerodynamics, engine, and beam models has demonstrated that it is capable of capturing key aspects of the complex flight behavior of both the air breathing and solid ablative rocket (SAR) modes of flight. These behaviors includes not just the expected precession and nutation behaviors anticipated for a spinning symmetric lightcraft body, but also capture the lightcraft's experimentally observed tendency to turn into the wind, and to orbit the center of the beam. This orbiting behavior was observed to either grow or decrease in radial distance depending on the initial conditions, and other factors such as crosswind. Figure 10 show how the computer model was able to well capture the nature of the light craft behavior for the first few seconds of the flight. At roughly 2 seconds into the flight the experimental results for this flight diverge from those predicted by the simulation because the lightcraft was caught by the wind and cast out of the beam once it cleared its protective

shielding. Additionally, the restoring impulse imparted to the lightcraft by the beam, which tends to push the lightcraft toward the center of the beam, drops off very rapidly beyond a certain radius (which varies with lightcraft height, and laser beam mirror spacing). When the lightcraft exceeded this radius during a flight, it would then "Frisbee" away from the beam.

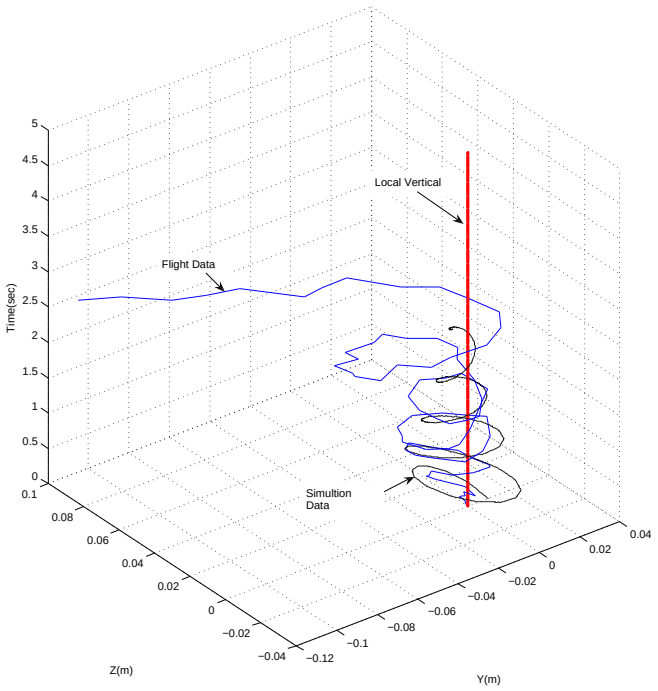

Figure 10: x-y-t model comparison of #200-5/6 SAR lightcraft in solid ablative rocket mode (flight 7)

5 Conclusions

Other than Libeau's proprietary software [9], no sufficiently robust flight dynamics code was available to guide lightcraft development into the future. The present version of the 7-DOF

code accurately predicts flight behavior of existing Type 200 lightcraft and is a significant milestone. Model-based predictive control is a necessity for lightcraft flight navigation with reduced nutation and precession. The lightcraft model presented here forms a cornerstone of the active controls effort.

Future improvements in the aerodynamic model will include Magnus forces upon spinning lightcraft in the presence of a crosswind. More accurate aerodynamic coefficients will shortly be forthcoming from subsonic wind tunnel tests of a full-scale #200-5/6 lightcraft, which will also consider non-steady flows. The engine model will be extended to include all Type 200 variations for which video flight data exists; experimental engine performance data currently is available for only the 200-3/4 (both SAR and air-breathing modes) and 200-11/10 (air-breathing mode only). Finally, the beam propagation model will be expanded to map the beam profile vs. range for various inverse telescopes of interest (i.e., using mirror separation as a parametric variable), as it evolves from the near-field region, through the focus, and into the far-field.

Acknowledgment

Support for this work by the National Science Foundation (NSF) under Award No. CMS-0219734, and the Air Force Office of Scientific Research (AFOSR) is gratefully acknowledged. Also, thanks is given to Dave Kenoyer and Ben Nagler class for their help in the present research.

References

[1] Myrabo, L., 2001, "World record flights of beam-riding rocket lightcraft: Demonstration of 'disruptive' propulsion technology," *37th AIAA/ASME/SAE/ASEE Joint Propulsion Conference.*, AIAA Paper N. 2001-3798, Salt Lake City, UT.

[2] Libeau, M. A., 2002, *Experimental Measurements of the Laser-Induced Reaction on a Lightcraft Engine*, Master's thesis, Rensselaer Polytechnic Institute, Troy NY.

[3] Kane, T. R., Levinson, D. A., and Likins, P. W., *Spacecraft Dynamics.*

[4] URL http://www.fluent.com/.

[5] Schaechter, D. B., Levinson, D. A., and Kane, T. R., 1982, *AUTOLEV User's Manual*, On-Line Dynamics Inc., Sunnyvale, CA.

[6] Kane, T. R. and Levinson, D. A., 1985, *Dynamics: Theory and Application*, Mcgraw-Hill, NY.

[7] Wiesel, W. E., 1989, *Spaceflight Dynamics*, McGraw Hill.

[8] URL http://www.solidworks.com.

[9] Libeau, M. A., Myrabo, L. N., and Filippelli, M., 1002, "Combined theoretical and experimental flight dynamics investigation of a laser propelled vehicle," *Proceedings of the First International Symposium on Beamed Energy Propulsion (ISBEP1)*, A. Pakhomov, ed., American Institute of Physics.

List of Figure Captions

1. Figure 1: Laser induced air plasma with type 100 lightcraft
2. Figure 2: Generic craft rotor system
3. Figure 3: Lightcraft aerodynamic loads diagram
4. Figure 4: Lightcraft aerodynamic drag coefficient vs. angle of attack
5. Figure 5: Lightcraft aerodynamic lift coefficient vs. angle of attack
6. Figure 6: Lightcraft aerodynamic moment coefficient vs. angle of attack
7. Figure 7: Characteristic vertical speed of #200-3/4 SAR lightcraft (simulation of flight 16)
8. Figure 8: Model comparison of #200-5/6 lightcraft in airbreathing PDE mode (flight 5)
9. Figure 9: Model comparison of #200-3/4SAR lightcraft in Solid Ablative Rocket (SAR) mode (flight 16)
10. Figure 10: x-y-t model comparison of #200-5/6 SAR lightcraft in solid ablative rocket mode (flight 7)
11. Table 1: Lightcraft parameters and flight conditions